physica **pssa** status solidi
www.pss-a.com

applications and materials science

Silicon nanocrystals: Novel synthesis routes for photovoltaic applications

Simon Perraud*,[1], Etienne Quesnel[1], Stéphanie Parola[1], Jérémy Barbé[1,2], Viviane Muffato[1], Pascal Faucherand[1], Christine Morin[1], Karol Jarolimek[3], René A. C. M. M. Van Swaaij[3], Miro Zeman[3], Stephen Richards[4], Andrew Kingsley[4], Hugh Doyle[5], Keith Linehan[5], Shane O'Brien[5], Ian M. Povey[5], Martyn E. Pemble[5], Ling Xie[6], Klaus Leifer[6], Kremena Makasheva[2,7], and Bernard Despax[2,7]

[1] CEA, LITEN, 17 rue des Martyrs, 38054 Grenoble Cedex 9, France
[2] Université de Toulouse, UPS, INPT, LAPLACE (Laboratoire Plasma et Conversion d'Energie), 118 route de Narbonne, 31062 Toulouse, France
[3] Photovoltaic Materials and Devices, Delft University of Technology, P.O. Box 5031, 2600 GA Delft, The Netherlands
[4] SAFC Hitech, Power Road, Bromborough, Merseyside, CH62 3QF, UK
[5] Tyndall National Institute, University College Cork, Lee Maltings, Cork, Ireland
[6] Department of Engineering Sciences, Uppsala University, Box 534, 751 21 Uppsala, Sweden
[7] CNRS, LAPLACE, 31062 Toulouse, France

* Corresponding author: e-mail simon.perraud@cea.fr, Phone: +33 4 38 78 26 08, Fax: +33 4 38 78 51 17

Novel processes were developed for fabricating silicon nanocrystals and nanocomposite materials which could be used as absorbers in third generation photovoltaic devices. A conventional high-temperature annealing technique was studied as a reference process, with some new insights in crystallisation mechanisms. Innovative methods for silicon nanocrystal synthesis at much lower temperature were demonstrated, namely chemical vapour deposition (CVD), physical vapour deposition (PVD) and aerosol-assisted CVD. Besides the advantage of low substrate temperature, these new techniques allow to fabricate silicon nanocrystals embedded in wide bandgap semiconductor host matrices, with a high density and a narrow size dispersion.

1 Introduction Silicon nanocrystals have been studied for a large range of applications, including single electron transistors, nonvolatile memories and so-called third generation solar cells [1]. Due to quantum confinement effects, the silicon nanocrystal bandgap can be tuned by changing the nanocrystal size or the host matrix properties. This fundamental property would allow the fabrication of highly efficient, low-cost multi-junction solar cells based on crystalline silicon materials.

The most widely employed technique for silicon nanocrystal synthesis is a two-step process, consisting of the thin film deposition of a silicon-rich material (typically silicon oxide or silicon nitride), followed by a high temperature annealing [2–4]. However, the annealing step at high temperature (generally above 1000 °C) represents a serious limitation for photovoltaic applications, since it precludes the use of low-cost substrates such as glass, metal or polymer. Therefore alternative methods for silicon nanocrystal synthesis are highly desirable, especially if they allow reducing process temperature and improving size control.

In this paper, we present novel routes for fabricating silicon nanocrystals and nanocomposite materials. This collaborative work, which involves several European research institutes and companies, has been performed within the framework of the European Union funded SNAPSUN project. First, we discuss a conventional high-temperature annealing technique (900–1100 °C), which is used as a reference process, with some new insights in crystallisation mechanisms. Then, we present innovative methods for silicon nanocrystal synthesis at much lower temperature: two dry processes (chemical vapour deposition (CVD) and physical vapour deposition (PVD)) and one wet process (solution synthesis of silicon nanocrystals followed by aerosol-assisted CVD of nanocomposite materials). We highlight several key advantages of these new processes.

(i) *Low substrate temperature*. The CVD process and the aerosol-assisted CVD process require a substrate temperature of 700 and 450 °C, respectively. The PVD process can be performed with a substrate at room temperature.

(ii) *High density of silicon nanocrystals with a well-defined diameter*. The new techniques presented in this article allow to fabricate silicon nanocrystals with a high density (higher than $1 \times 10^{12} \, cm^{-2}$) and a narrow size dispersion (mean diameter lower than 5 nm and standard deviation down to 15%).

(iii) *Semiconducting host matrices*. In order to achieve nanocomposite materials with an electrical conductivity suitable for photovoltaic applications, this paper focuses on the fabrication of silicon nanocrystals embedded in semiconducting host matrices (such as silicon carbide, zinc oxide or indium oxide), instead of conventional electrically insulating host matrices (silicon oxide or silicon nitride).

2 High temperature annealing process

2.1 Experimental details A series of amorphous silicon carbide (SiC) samples with varying carbon content were deposited using plasma enhanced chemical vapour deposition (PECVD) at a frequency and power density of 13.56 MHz and 139 mW cm^{-2}, respectively. Films were deposited on quartz substrates at a temperature of 500 °C. Process pressure and total gas flow were fixed at 1.4 mbar and 102 sccm. In order to prepare films with different carbon content, a series of methane-to-silane ratios was used: 2.0, 2.7, 4.0, 5.7, 9.0, 13.4, 23.9, and 50.0. X-ray photoemission spectroscopy measurements reveal that the last gas ratio results in close to stoichiometric material with composition: $Si_{0.44}C_{0.48}O_{0.08}$. Due to the high substrate temperature the films do not contain hydrogen. Annealing was performed in a conventional furnace with N_2 atmosphere. The samples were placed in a preheated furnace and after annealing placed on a metal surface to cool. Raman spectra were measured on a Renishaw inVia microscope with a 514 nm laser.

2.2 Results and discussion As can be seen in Fig. 1(a) the as-deposited layers are heterogeneous. The excess silicon forms silicon nanoparticles that are amorphous, as evidenced by the diffuse rings in the Fourier transform of the high resolution transmission electron microscopy (TEM) image. Also Raman spectra show a purely amorphous material. Several researchers, using H_2 dilution and higher powers, report formation of crystalline silicon nanoparticles in as-deposited material [5, 6].

As-deposited films were subsequently annealed at high temperatures (900, 1000 and 1100 °C) to study the crystallisation of amorphous silicon nanoparticles. In Fig. 1(b) we show a high resolution TEM image of SiC film prepared with gas ratio 9 after it was annealed for 1 h at 1100 °C. The film contains crystalline silicon with (022) and (113) reflections clearly visible in the Fourier transform image.
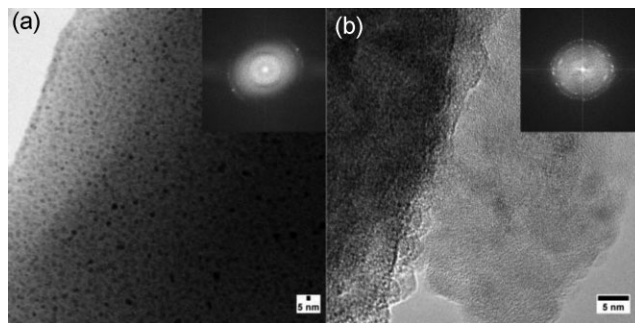

Figure 1 TEM images of films prepared with a methane to silane ratio equal to 9. (a) Bright field image of the as-deposited film. (b) High resolution image of a film annealed for 1 h at 1100 °C. The insets were generated by a Fourier transform of high resolution images.

In order to study the transformation from amorphous to crystalline silicon in SiC films we record Raman spectra. Amorphous silicon gives rise to a broad TO peak located at 480 cm^{-1}, whereas crystalline silicon induces a sharp peak at 520 cm^{-1}. In the following we will use the ratio of crystalline to amorphous peak intensities as a measure for the crystallinity in the film. Figure 2 depicts the crystallisation kinetics of a series of films with different carbon content annealed at 1100 °C.

Within the first 2 h the phase transformation advances fast. After that the process slows down, although it does not stop even after 6 h. We also observe that increasing the amount of carbon will inhibit silicon crystallisation. Excess silicon in the film prepared with methane to silane ratio of 23.9 stays in the amorphous phase even after an 18 h anneal. The film prepared with gas ratio of 50.0 does not contain Si–Si vibrational modes in the spectra and is thus either stoichiometric or slightly carbon rich. Annealing at lower temperatures results in overall lower crystallinity ratios. For example, an 18 h anneal of SiC (gas flow ratio 2.0) at
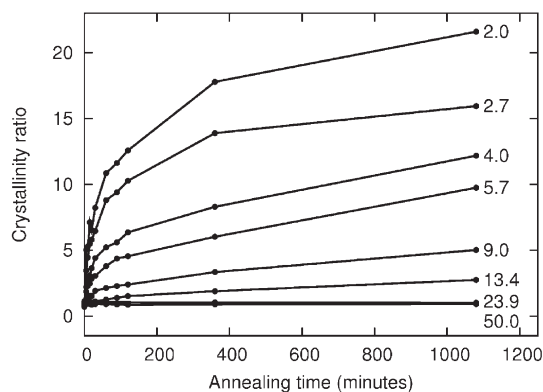

Figure 2 Crystallisation kinetics of amorphous SiC films with different carbon content, annealed at 1100 °C. The crystallinity ratio is plotted against annealing time, for different methane-to-silane ratios.

Original

Paper

Phys. Status Solidi A 210, No. 4 (2013)

651

1000 °C results in a crystallinity ratio around 9, while for annealing at 900 °C this ratio is only ~4. For comparison, the melting temperature of Si in crystalline SiC, according to the phase diagram, is 1414 °C [7]. A possible explanation for the large differences in crystallinity between the ratios is that the crystallisation temperature is size dependent [8]. This implies that at lower temperatures only a fraction of the nanoparticles will crystallise.

To sum up, we have prepared crystalline silicon nanoparticles embedded in SiC matrix. We find that the as-deposited SiC films contain amorphous silicon nanoparticles to begin with. A systematic study of the crystallisation of nanoparticles reveals that the process is inhibited by an increased carbon content. Annealing experiments conducted at temperatures well above 1100 °C are probably necessary to fully understand the crystallisation process.

3 Chemical vapour deposition process Direct nucleation and growth by a CVD process is a promising method to synthesise silicon nanocrystals, due to lower substrate temperature compared to the standard annealing technique described in the previous section. Baron et al. have shown the possibility to fabricate silicon nanocrystals onto electrically insulating substrates by controlling the early stage of the silicon growth in a CVD reactor [9]. They have obtained a high density of nanocrystals, up to 10^{12} cm^{-2} on silicon oxide and silicon nitride, and have shown that the chemical nature of the substrate has a strong influence on the nucleation rate. A similar technique has been developed in the present work for the case of semiconducting substrates, namely amorphous silicon carbide thin films.

3.1 Experimental details Amorphous silicon carbide thin films were deposited by PECVD (13.56 MHz capacitively coupled discharge maintained at total pressure of 4 Torr with power density of 162 mW cm^{-2}) on silicon substrates kept at 200 °C during the deposition. Then, samples were transferred to a low pressure CVD reactor. Since in our experimental set-up the PECVD reactor for amorphous silicon carbide thin film deposition and the CVD reactor for silicon nanocrystal growth are two different tools, the samples were exposed to air between the PECVD process and the CVD process. The amorphous silicon carbide films were treated by 10%-HF for 10 s in order to remove the surface native oxide and to hydrogenate the surface just before the silicon nanocrystal growth. We observed that this HF treatment is essential to obtain a high density of silicon nanocrystals. Silicon nanocrystal nucleation and growth onto the amorphous silicon carbide surface was carried out by thermal decomposition of silane in hydrogen at 700 °C under a total pressure of 20 Torr. Silicon nanocrystals were formed on the amorphous silicon carbide surface by using low silane gas flow rate for short growth time. It was verified that the silicon carbide thin film remains amorphous after the silicon nanocrystal growth step, and that there is no silicon nanocrystals formed inside the

amorphous silicon carbide layer. More details on this part of the study and a thorough analysis of the results are given elsewhere [10].

3.2 Results and discussion In order to show our ability to control silicon nanocrystal density and size, two sets of samples with various silane flow rates and growth time were prepared. An a-Si$_{0.8}$C$_{0.2}$ layer with well-defined properties was selected as host surface. It can be seen in Fig. 3 that the silicon nanocrystal density increases as the growth time or the silane flow rate increases. We observe the same variations for the silicon nanocrystal mean diameter: all along the process, the silicon nanocrystals grow until coalescence for either high silane flow rate or long growth time.

We have observed that, for the same growth time and silane flow rate, the silicon nanocrystal density is almost 10 times higher for growth onto the surface of a PECVD-deposited amorphous silicon carbide (a-Si$_{0.8}$C$_{0.2}$) thin film than onto the surface a thermally grown silicon oxide thin film. For example, at a growth temperature of 700 °C, a growth time of 15 s and a SiH$_4$ flow rate of 20 sccm, the silicon nanocrystal densities found on a-Si$_{0.8}$C$_{0.2}$ and SiO$_2$ surfaces are about 8×10^{11} and 5×10^{10} cm^{-2}, respectively. This large difference can have several origins. First, Si–H and C–H bonds have smaller bond energies (70 and 97.9 kcal mol^{-1}, respectively) than the O–H bond energy (102 kcal mol^{-1}). After an HF treatment, the silicon oxide surface is partly terminated by silanol groups while the a-Si$_{0.8}$C$_{0.2}$ surface has a majority of Si–H and C–H terminations that promote the slicon nanocrystal nucleation by chemical reactions. Second, it has been observed that
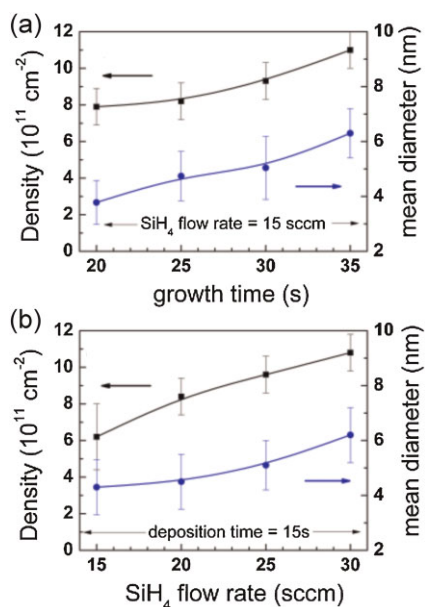
Figure 3 (online colour at: www.pss-a.com) Variations of density and mean size of silicon nanocrystals grown on a-Si$_{0.8}$C$_{0.2}$ at 700 °C as a function of growth time (a) and silane flow rate (b). Lines are shown as guide to the eye.

PECVD-deposited thin films enhance the silicon nanocrystal nucleation compared to thermally grown silicon oxide [11], which is due to a higher degree of dangling bonds and defects at the layer surface, as well as to a higher surface roughness. Third, the a-$Si_{0.8}C_{0.2}$ layer has a higher silicon concentration (90% mass concentration) than the silicon oxide layer (46% mass concentration). The silicon atoms are known to be preferential nucleation sites for silane radicals, which makes the silicon rich carbide layer a preferential surface for the nucleation of silicon nanocrystals.

TEM-based techniques were used in order to better understand the size distribution and the crystalline structure of the silicon nanoparticles. In Fig. 4(a), silicon nanoparticles appear as dark circular contrast in the bright field TEM image with a high density of $1.3 \times 10^{12} cm^{-2}$. From the same image, we determined the size distribution for a sample group of 49 nanoparticles. Only isolated nanoparticles were taken into account in this study although a significant amount of agglomerates are visible on the surface. The histogram in Fig. 4(b) gives a mean diameter of 4.8 nm and a very small standard deviation of 0.7 nm. Figure 4(c) shows high resolution TEM plan-view image of one nanoparticle at high magnification. The nanoparticle has (200) lattice planes visible. In the selective area diffraction pattern shown in Fig. 4(d), silicon nanoparticle reflections of Si (200) and (111) lattice planes are observed. It indicates

that silicon nanoparticles do not have any preferential orientation with respect to the substrate plane. These observations clearly show that the silicon nanoparticles grown on a-$Si_{0.8}C_{0.2}$ thin films by CVD at 700 °C are crystalline.

4 Physical vapour deposition process One challenging and relatively cost-effective alternative to CVD-grown silicon nanocrystals described in the previous section is the synthesis of nano-aggregates by inert-gas condensation of a sputtered vapour in a dedicated magnetron-based reactor [12]. By tuning the collision path length and hence the time of residence of nanoparticles in the carrier gas phase, spherical aggregates with well-controlled nanometer-scale diameters and relatively narrow size dispersion can be produced from various materials, metals or semiconductors. The unique characteristic of this technological route is that the crystallisation of the nanocrystals occurs in the inert-gas phase of the nanoparticle source, precisely before their deposition on the substrate. In other words, contrary to CVD processes, no heating of substrate is required, making this PVD technology particularly interesting for photovoltaic applications with temperature sensitive glass or polymer substrates.

4.1 Experimental details A detailed description of process has been previously given elsewhere for Cu and Pt-based alloys [13] as well as germanium nanoparticles [14]. The nanoparticle source was connected to a main deposition chamber used for the nanocomposite host matrix deposition by ion beam sputtering. Successive or simultaneous deposition of silicon nanoparticles and/or oxide matrix is then possible on a same substrate kept at room temperature. Two matrices were studied, silicon oxide (SiO_2) as an electrically insulating matrix, and aluminium doped zinc oxide (ZnO:Al) as a wide band gap semiconductor matrix.

4.2 Results and discussion Figure 5(a) presents typical absorption spectra ($A = 1 - R - T$) of nanocomposite materials made of silicon nanocrystals in silicon oxide or ZnO:Al host matrices. In both cases, the nanocrystal surface density is around $10^{13} cm^{-2}$, with a mean nanocrystal size of 3.0 ± 0.5 nm. We observe that within silicon oxide the silicon nanocrystals induce a strong visible absorption in comparison with SiO_2 matrix alone (see 'SiO_2' curve and 'Silica + Si nanocrystals' curve). The determination of the optical band gap using the well-known Tauc formula gives a value of 2.15 eV and shows how the silicon crystal size reduction induces a strong quantum confinement with a much higher optical band gap than that of bulk silicon [Fig. 5(b)]. This band gap value was confirmed by photoluminescence measurements, with a light emission peak at 2.15–2.2 eV. On the contrary, within ZnO:Al, the silicon nanocrystals only induce weak additional absorption (in the 400–500 nm range) despite their relatively high surface density.
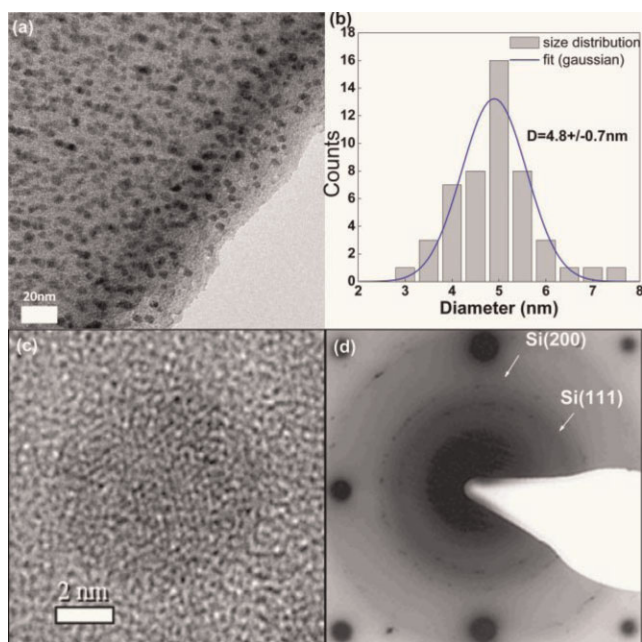

Figure 4 (online colour at: www.pss-a.com) Plan-view TEM observations of silicon nanocrystals grown on a-$Si_{0.8}C_{0.2}$ surface. (a) Bright field TEM image. (b) Size distribution determined from (a) for isolated silicon nanocrystals. (c) Plan-view high resolution TEM image at high magnification. (200) planes of silicon nanocrystals are observed. (d) Selective area diffraction pattern shows the diffraction pattern of silicon substrate on [100] zone axis as well as Si(200) and Si(111) reflections from the silicon nanocrystals.
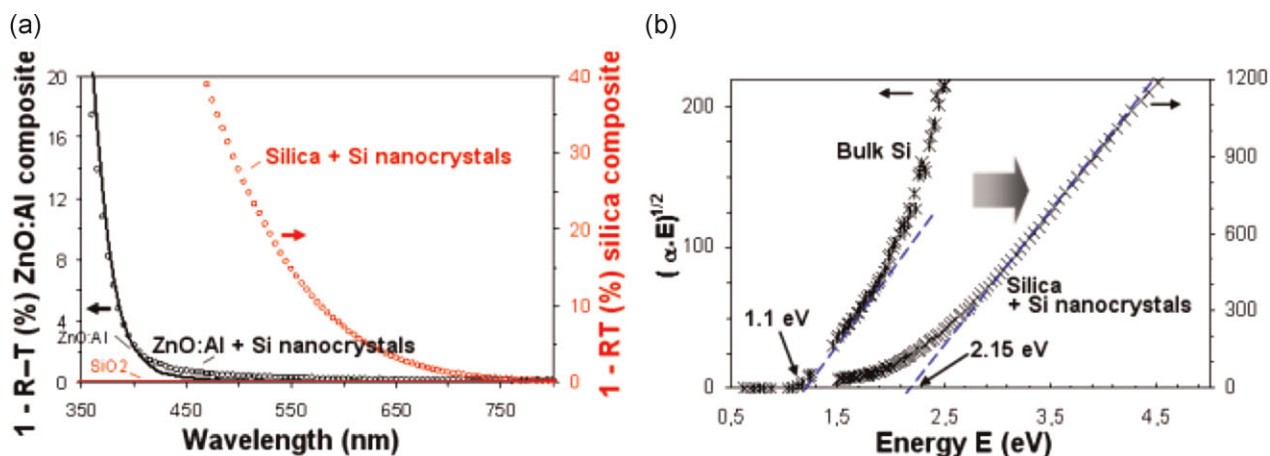
Original

Paper

Phys. Status Solidi A 210, No. 4 (2013)

653

Figure 5 (online colour at: www.pss-a.com) (a) Absorption curves of silicon nanocrystals in ZnO:Al or SiO$_2$ matrices with reference matrix. (b) Comparison between the Tauc optical bandgap of nanocomposite and crystalline silicon substrate.

TEM characterisations done on the same sample evidence that most silicon nanocrystals actually turn into silica nanoparticles (no longer absorbing) by oxidation within the composite. This result is consistent with thermodynamics considerations (Ellingham diagrams) which predict that SiO$_2$ is more stable than ZnO. A first analysis of TEM image of a nanocomposite made of silicon nanocrystals in a ZnO:Al host matrix [Fig. 6(a)] shows that the nanocomposite layer contains indeed a matrix (bright contrast) with a large number of nanoparticles (dark contrast). Increasing the magnification by an order of magnitude reveals three kinds of nanoparticles coexisting in the layer [Fig. 6(b)], hexagonal shaped ZnO:Al crystals, dark contrasted Si nanocrystals (at the bottom of image) and SiO$_2$ nanoparticles found to attach to the ZnO nanoparticles.

Building a nanocrystal-based solar cell requires understanding how the nanocomposite absorber can be integrated in a photovoltaic junction. For that purpose, a PVD nanocrystal-based solar absorber was first prepared and integrated into a p–i–n semiconductor junction. It obviously raises tremendous issues mostly dealing with electrical concerns like (i) the capacity to form an operating junction within the nanocomposite layer and (ii) the ability to collect the photo-generated charge carriers.
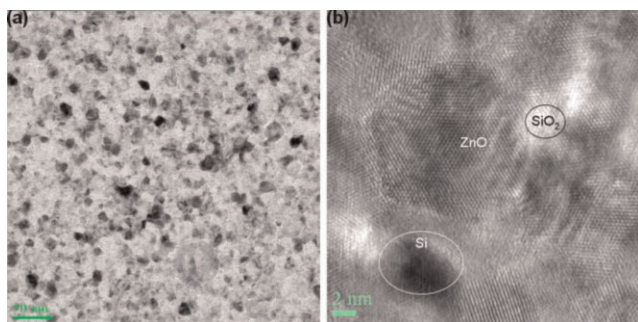
As first indications of how challenging this issue is, we present in Fig. 7 preliminary rough photovoltaic measurements obtained with as-deposited PVD germanium nanocrystals. No curing or passivation procedure was applied on the sample. Germanium nanocrystals were preferred the silicon nanocrystals because of their better stability with respect to ZnO:Al host matrix. Figure 7 shows an external quantum efficiency curve of the simple photovoltaic device described in the inset. At first glance, the measured photovoltaic current would result from electron–hole pairs generated inside the nanocrystals demonstrating the possibility to integrate a PVD nanocrystal-based composite absorber into a photovoltaic devise. However, the current–voltage curve recorded under AM1.5 sun irradiation gives poor electrical characteristics with an open circuit voltage of 33 mV, a short circuit current of 0.08 mA cm^{-2} and a fill factor of 0.28. These very low values are caused by the high electrical leakage inside the porous nanocomposite and the very high recombination rate. They underline the necessity
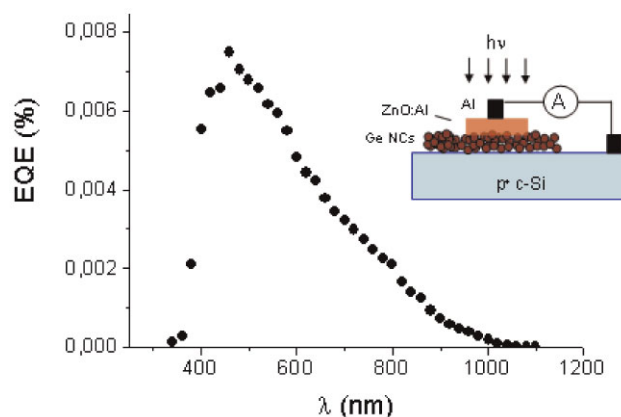

Figure 6 (a) Bright field TEM image at 63k magnification, (b) high resolution TEM image at 500k magnification.

Figure 7 (online colour at: www.pss-a.com) External quantum efficiency curve measured on the nano-PV device presented in the inset.

to further work on the nanocomposite microstructure and to implement dedicated passivation strategies.

5 Wet process Compared to the dry processes described above, wet processes may significantly reduce the fabrication cost of silicon nanocrystals and nanocomposite materials. Chemical solution deposition (CSD) methods have been attracting increasing attention in recent years in the development of processes for coating large-area substrates using low cost technologies compatible with high volume industrial production. CSD techniques can generally be categorised as either liquid (spin or dip coating) or spray (spray pyrolysis/aerosol-assisted CVD). For oxide coating processes, liquid methods are generally favoured where possible, due to the comparatively lower costs involved in the coating process. However, for other more complex processing, *e.g.* in situations where further doping with specifically functionalised nanoparticles is required for the end-user application, spray methods can offer advantages which justify the increased cost and complexity involved. Spin and dip coating of nanoparticle loaded solutions is generally problematic, in the case of ligand stablilised nanoparticles due to dilution greatly reducing the nanoparticle concentration on the substrate surface and in the case of nanopowders it is observed that even additions of small quantities of powders result in the formation of a paste which cannot be uniformly coated onto a substrate. However, in the case of spray methods, compatible host matrices and nanoparticle dispersion can be co-deposited in a controlled manner. In aerosol-assisted CVD, droplets of liquid precursors are generated and carried into the hot-zone of a furnace where the solvent evaporates and the host matrix precursor (and nanoparticles if present) is deposited onto a substrate. This lends itself to the growth of nanocomposite films adding enhanced functionality to the host matrix systems used.

In the present work, we have used of a novel precursor chemical for the growth of indium tin oxide (ITO), which is compatible with ligand stabilised dispersions of silicon nanoparticles which have been synthesised by the reverse-micelle method. The advantage of using these nanoparticles is that they are synthesised separately and can be characterised prior to use to ensure that they meet the requirements of the nanocomposite material end-user.

However, it is important to note that process development to incorporate these silicon nanoparticles requires a different approach to that which is currently used in aerosol-assisted CVD/spray methods. A key requirement is that the host matrix precursor and ligand stabilised dispersions of silicon nanoparticles mix homogenously, without the occurrence of chemical reactions which could lead to turbidity or precipitation. With that in mind, it was decided that the indium and tin source chemicals employed should be soluble in an organic solvent that is miscible with hexane (the solvent system best suited to synthesis of silicon nanocrystals with a narrow, tunable particle size distribution). This approach varies from reported accounts of aerosol and spray growth of ITO, as they generally use polar solvent, which are not compatible with silicon nanocrystals dispersed in hexane.

5.1 Solution synthesis of silicon nanocrystals
5.1.1 Experimental details
The synthesis of the silicon nanocrystals is adapted from the method reported by Tilley and coworkers [15]. All reagents and solvents were purchased from Sigma–Aldrich Ltd. and used as received. In a nitrogen filled glove-box, 1.5 g of tetraoctylammonium bromide (TOAB) was dissolved in 100 mL anhydrous toluene. 1 mL (0.008 mol) $SiBr_4$ was added to the above solution and the mixture was left to stir for 30 min. Silicon nanocrystals were then formed by the dropwise addition of 6 mL of 1 M lithium aluminium hydride in THF over a period of 2–4 min. The solution was then left to react for 2.5 h. The excess reducing agent was then quenched with the addition of 60 mL methanol, upon which the dispersion became transparent. At this stage of the reaction the silicon nanocrystals are terminated by hydrogen and encapsulated in a TOAB micelle.

Chemically passivated nanocrystals were then formed by modifying the silicon–hydrogen bonds at the surface through addition of 200 µL of a 0.1 M H_2PtCl_6 in isopropyl alcohol as a catalyst followed by 6 mL of 1-heptene. After stirring for 2.5 h, silicon nanocrystals were removed from the glove box and the organic solvent removed by rotary evaporation. The resulting dry powder (consisting mainly of TOAB) was then redispersed in 20 mL of hexane and sonicated for 30 min.

The solution was then filtered twice using PVDF membrane filters (MILLEX-HV, Millipore 0.45 µM) to remove surfactant, after which it was washed with 100 mL of *n*-methyl formamide (four times) and with distilled water. Pure silicon nanocrystals capped with 1-heptene remain in the hexane phase. The solution was concentrated down to 1 mL and placed into the column (1, 41.0 cm). Sephadex gel LH-20 was used as the stationary phase and fractions were collected every 50 drops at a flow rate of a drop every 5 s. A hand held UV lamp (365 nm) was used to check each fraction for silicon nanocrystal luminescence. The fractions were then combined and reduced to a total volume of 20 mL.

UV–Vis absorption spectra were recorded using a Shimadzu UV PC-2401 scanning double beam spectrophotometer equipped with a 60 mm diameter integrating sphere (ISR-240A, Shimadzu). Absorption spectra were recorded at room temperature using a quartz cuvette (1 cm) and corrected for the solvent absorption. Photoluminescence spectra with excitation wavelengths ranging from 320 to 400 nm were recorded on a Perkin Elmer LS 50 luminescence spectrophotometer equipped with a pulsed Xenon discharge lamp and Monk-Gillieson monochromators. Infrared spectra were recorded on a Biorad FTS 3000 spectrometer. Samples were formed by placing an aliquot of silicon nanocrystals dispersed in hexane onto NaCl plates, after which the sample was allowed to evaporate to dryness. TEM analysis was carried out using a JEOL 2100 electron

Phys. Status Solidi A 210, No. 4 (2013)

655

microscope operating at 200 kV and equipped with an LAB$_6$ electron source. TEM samples were prepared by depositing number of aliquots of colloidal silicon nanocrystal solution, 300 μL in total, onto a carbon coated TEM grid. The solvent was allowed to completely evaporate between successive depositions.

5.1.2 Results and discussion Figure 8 shows a representative TEM image of the heptene-capped silicon nanocrystals, showing the range of nanocrystal sizes observed. From the image, it is clear that the silicon nanocrystals were relatively monodisperse, with no evidence of aggregation. Inset in Fig. 8 is the histogram of the silicon nanocrystal diameters, determined by analysis of TEM images of ca. 120 nanocrystals located at different regions of the grid. The average nanocrystal diameter is 3.0 ± 0.4 nm (0.4 nm being the standard deviation), which highlights the highly monodisperse size distribution synthesised. Selected area electron diffraction patterns showed reflections consistent with cubic crystalline silicon. Energy dispersive X-ray spectroscopy also confirmed the presence of silicon.

The silicon nanocrystals were further characterised by infrared spectroscopy, see Fig. 9, which exhibits clear C–H stretching signals, with the symmetric CH$_2$, asymmetric CH$_2$ and the asymmetric C–CH$_3$ stretching vibrations at 2860, 2926 and 2960 cm^{-1}, respectively. The presence of the peak at 1462 cm^{-1}, assigned to the Si–C scissoring vibration, shows the covalent attachment of 1-heptene molecules to the surface of the H-terminated silicon nanocrystals [16]. The peak at 1379 cm^{-1} is assigned to the C–CH$_3$ symmetrical bending mode. The peaks between 1000 and 1100 cm^{-1} are attributed to Si–OR stretching modes. The low intensity of these peaks indicates that only minimal oxidation of the silicon core has taken place, as this is typically a strong signal due to the polarity of the Si–O bond [16].
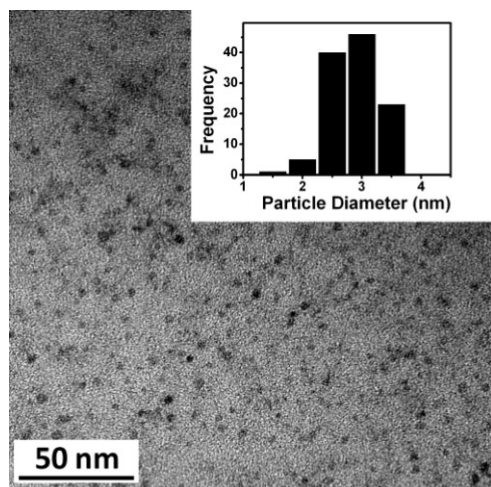

Figure 8 TEM image of heptene-terminated silicon nanocrystals. A histogram of nanocrystal core diameters is shown inset.
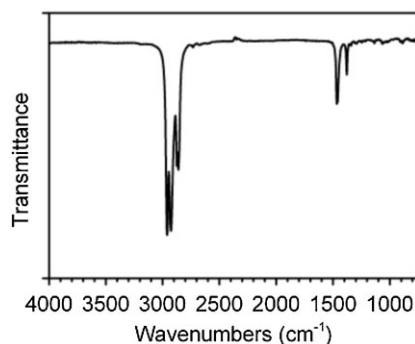

Figure 9 Fourier transform infrared spectrum of heptene-terminated silicon nanocrystals.

Figure 10 presents the absorbance and photoluminescence spectra (280 nm excitation) of the 1-heptene capped silicon nanocrystals dispersed in hexane. The absorption spectrum shows a broad absorbance band centred at 264 nm, in good agreement with other reports [17, 18]. The photoluminescence spectrum, obtained using an excitation wavelength of 280 nm, showed a peak at ca. 340 nm (3.65 eV), in good agreement with previous reports of silicon nanocrystals of similar size [17, 18].

It is noted that the absorbance spectrum for the silicon nanocrystals is considerably blue-shifted from that observed for nanocrystals prepared by PVD (see Fig. 5). This is most likely due to the presence of the heptene passivation layer, which prevents oxidation of the surface of the nanocrystals, compared to the PVD-grown nanocrystals, which do have an oxidised surface. It is known from theoretical studies that the LUMO of the nanocrystals is centred much more on the surface than the HOMO, so that alterations to surface of silicon nanocrystals can have significant effects on their photophysical properties [19]. Density functional calculations on silicon nanoclusters have shown that surface oxidation results in decreasing the band gap by more than 1 eV [20, 21], which is consistent with the differences in the photophysical properties observed for solution synthesised and PVD-grown nanocrystals.
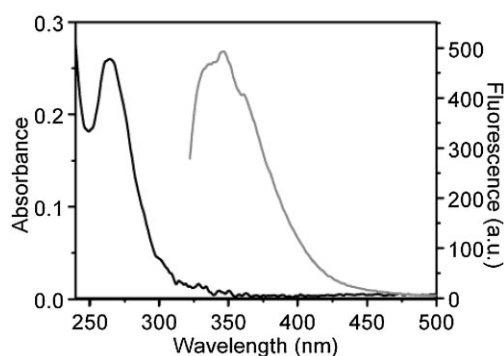

Figure 10 UV–Vis absorbance (black line) and photoluminescence (grey line) spectra of silicon nanocrystals dispersed in hexane.

5.2 Aerosol-assisted chemical vapour deposition of nanocomposite materials

5.2.1 Experimental details A 25% solution of indium and tin neodecanoate in xylene (SAFC Hitec) was used to grow ITO by aerosol-assisted CVD. In this work the indium and tin sources were specifically chosen to be soluble in an organic solvent which would be compatible with a wide range of ligand stabilised nanoparticles, in order to enable further work in nanocomposite material film growth. Aerosol-assisted CVD films were deposited using a modified CVD system consisting of a tubular quartz reactor containing a graphite susceptor. 20 mL of solution held in a container above the metal diaphragm of a modified commercially available ultrasonic humidifier to form an aerosol, was used as the precursor. The aerosol generated was swept into the reaction zone using a nitrogen carrier gas ($1.58\,L\,min^{-1}$) metered from a mass flow controller. Films were prepared from a precursor solution consisting of a 1:5 ratio of ITO (neodecanoate): silicon nanocrystal dispersion. Films were grown at $450\,°C$ on quartz and silicon wafer substrates containing a native oxide on the surface. Samples were cleaned in acetone and isopropyl alcohol and dried in flowing nitrogen immediately prior to use.

5.2.2 Results and discussion Different TEM techniques were used to characterise the nanocomposite materials synthesised by wet chemical methods. In Figure 11(a), the high resolution TEM image gives a general view of silicon nanoparticles and the dark contrast indicates nanoparticles. However, the phase contrast of nanoparticles in Fig. 11(a) is difficult to interpret, therefore,

we use annular dark field imaging in a scanning transmission electron microscope (STEM-ADF) to characterise the nanoparticles synthesised by wet chemical methods. STEM-ADF technique uses incoherent scattered electrons to form images, and the contrast is strongly correlated with specimen atomic number and surface morphology. In Fig. 11(b), STEM-ADF image shows nanoparticles with bright contrast. The size distribution and density of nanoparticles were measure from Fig. 11(b). The nanoparticles have a size distribution of $3.1 \pm 0.8\,nm$ and a density of about $4 \times 10^{12}\,cm^{-2}$.

6 Conclusions Novel processes were developed for fabricating silicon nanocrystals and nanocomposite materials which could be used as absorbers in third generation photovoltaic devices. A conventional high-temperature annealing technique was studied as a reference process, with some new insights in crystallisation mechanisms. Innovative methods for silicon nanocrystal synthesis at much lower temperature were demonstrated, namely CVD, PVD and aerosol-assisted CVD. Besides the advantage of low substrate temperature, these new techniques allow to fabricate silicon nanocrystals embedded in wide bandgap semiconductor host matrices, with a high nanocrystal density (higher than $1 \times 10^{12}\,cm^{-2}$) and a narrow nanocrystal size dispersion (mean diameter lower than $5\,nm$ and standard deviation down to 15%). Ongoing work focuses on integrating the nanocomposite materials into solar cells, in order to evaluate their potential for photovoltaic applications.
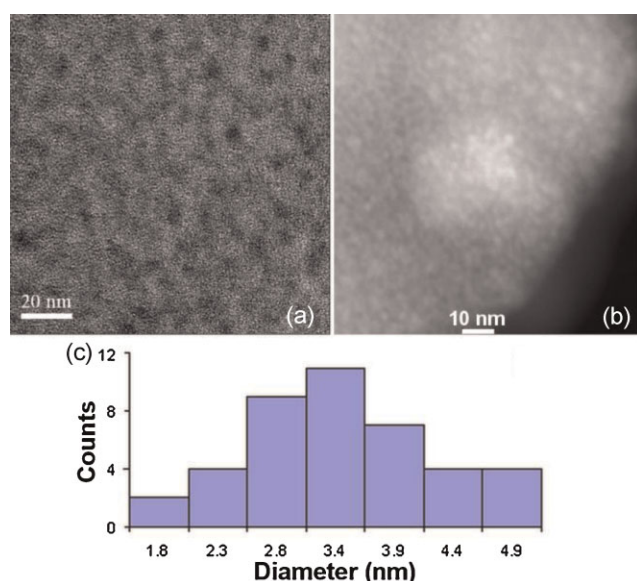
Figure 11 (online colour at: www.pss-a.com) (a) High resolution TEM image on a typical sample. (b) STEM-ADF image showing the nanoparticles (the scale bar is 10 nm). (c) Size distribution of nanoparticles.

References

[1] G. Conibeer, C. Jiang, D. König, S. Shrestha, T. Walsh, and M. Green, Thin Solid Films **516**, 6968 (2008).

[2] S. Perret-Tran-Van, K. Makasheva, B. Despax, C. Bonafos, P. E. Coulon, and V. Paillard, Nanotechnology **21**, 285605 (2010).

[3] Y. Kurokawa, S. Miyajima, A. Yamada, and M. Konagai, Jpn. J. Appl. Phys. **45**, 1064 (2006).

[4] M. Künle, T. Kaltenbach, P. Löper, A. Hartel, S. Janz, O. Eibl, and K. G. Nickel, Thin Solid Films **519**, 151 (2010).

[5] Q. Cheng, E. Tam, S. Xub, and K. Ostrikov, Nanoscale **2**, 594 (2010).

[6] U. Coscia, G. Ambrosone, and D. K. Basa, J. Appl. Phys. **103**, 063507 (2008).

[7] K. Korniyenko, The Landolt-Börnstein Database, New Series IV/11E1 (Springer-Verlag, Berlin, Heidelberg, 2009).

[8] M. Hirasawa, T. Orii, and T. Seto, Appl. Phys. Lett. **88**, 093119 (2006).

[9] T. Baron, F. Martin, P. Mur, C. Wyon, and M. Dupuy, J. Cryst. Growth **209**, 1004 (2000).

[10] J. Barbé, L. Xie, K. Leifer, P. Faucherand, C. Morin, D. Rapisarda, E. De Vito, K. Makasheva, B. Despax, and S. Perraud, Thin Solid Films, in press, http://dx.doi.org/10.1016/j.tsf.2012.08.046.

Original Paper

Phys. Status Solidi A 210, No. 4 (2013)

657

[11] J. T. Fitch, J. Electrochem. Soc. **141**, 1046 (1994).

[12] A. H. Kean and L. Allers, in: Technical Proceedings of the 2006 NSTI Nanotechnology Conference and Trade Show, Vol. 1, Boston, MA, 2006, pp. 749–752.

[13] E. Quesnel, E. Pauliac-Vaujour, and V. Muffato, J. Appl. Phys. **107**, 054309 (2010).

[14] S. Parola, E. Quesnel, V. Muffato, O. Raccurt, L. Guetaz, and A. Slaoui, in: Proceedings of the 25th European Photovoltaic Solar Energy Conference, Valencia, Spain, 2010.

[15] R. D. Tilley, J. H. Warner, K. Yamamoto, I. Matsui, and H. Fujimori, Chem. Commun. 1833 (2005).

[16] M. Rosso-Vasic, E. Spruijt, B. van Lagen, L. De Cola, and H. Zuilhof, Small **4**, 1835 (2008).

[17] N. Shirahata, T. Hasegawa, Y. Sakka, and T. Tsuruoka, Small **6**, 915 (2010).

[18] J. Wang, S. Sun, F. Peng, L. Cao, and L. Sun, Chem. Commun. **47**, 4941 (2011).

[19] A. Puzder, A. J. Williamson, F. A. Reboredo, and G. Galli, Phys. Rev. Lett. **91**, 1574051 (2003).

[20] Z. Zhou, L. Brus, and R. Friesner, Nano Lett. **3**, 163(2003).

[21] A. Puzder, A. J. Williamson, J. C. Grossman, and G. Galli, Phys. Rev. Lett. **88**, 097401 (2002).